

Dirac fermions in half-metallic ferromagnetic mixed $\text{Cr}_{1-x}\text{M}_x\text{PSe}_3$ monolayers

Juntao Yang,^{1,2} Yong Zhou,¹ Yuriy Dedkov,^{1,*} and Elena Voloshina^{1,†}

¹*Department of Physics, Shanghai University,*

99 Shangda Road, 200444 Shanghai, China and

²*School of Science, Hubei University of Automotive Technology,*

167 Checheng West Road, Shiyan City, 442002 Hubei, China

(Dated: December 23, 2021)

Abstract

The electronic and magnetic properties of pristine CrPSe_3 and mixed $\text{Cr}_{1-x}\text{M}_x\text{PSe}_3$ ($\text{M} = \text{Zn}, \text{Cd}, \text{Hg}$) monolayers were studied using density functional theory including an on-site Coulomb term (DFT+ U) and tight-binding approach (TBA). While pristine CrPSe_3 monolayer has an antiferromagnetic (AFM) ground state, its alloying with MPSe_3 may give rise to half-metallic ferromagnet (HMF) with high Curie temperature. The resulting monolayers demonstrate single-spin Dirac cones of mainly Cr- d character located in the first Brillouin zone directly at the Fermi energy. The calculated Fermi velocities of Dirac fermions indicate very high mobility in mixed $\text{Cr}_{1-x}\text{M}_x\text{PSe}_3$ monolayers, that makes this material appealing for low-dimensional spintronics applications.

* E-mail: dedkov@shu.edu.cn

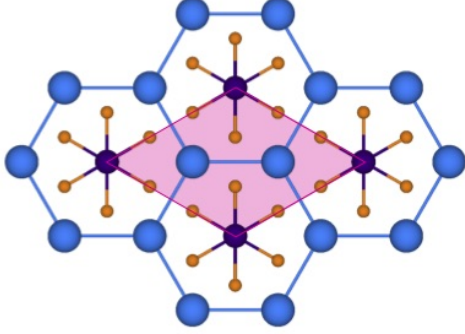
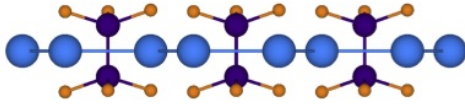
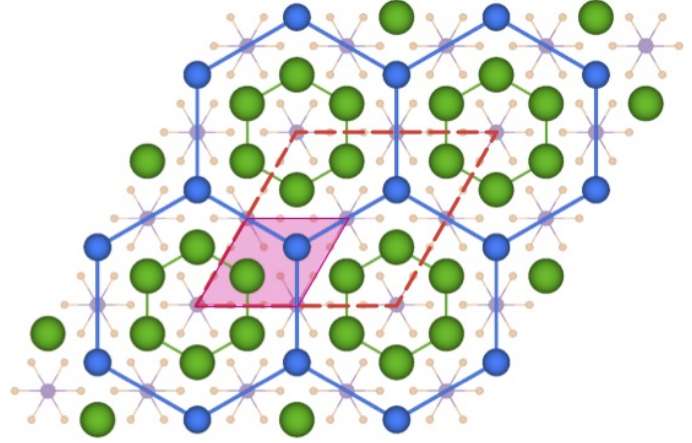
† E-mail: voloshina@shu.edu.cn

Discovery of the fascinating transport properties of graphene [1–3] stimulated the enormous interest to the family of two-dimensional (2D) materials, leading to the success in the synthesis or exfoliation from bulk of different 2D materials, like *h*-BN [4–6], black phosphorene [7], silicene [8, 9], transition-metal dichalcogenides [10, 11] and many others. Here, the electronic structure is ranged from metallic (graphene, silicene) to insulating (*h*-BN) state. Although a great quantity of 2D crystals have been widely explored, most of them are lacking of intrinsic ferromagnetic (FM) ordering. Inspired by the discovery of layer-dependent ferromagnetism in insulating CrI₃ monolayer with a Curie temperature (T_C) of 45 K [12], many 2D magnetic materials have been recently synthesized, such as semiconducting Cr₂Ge₂Te₆ [13], its metallic analogue Fe₃GeTe₂ [14], and semiconducting MnSe₂ [15], initiating enormous attention to the field of magnetic 2D atomic crystals [16, 17]. Meanwhile, some novel properties have been also predicted for the 2D magnetic materials, e. g. the Dirac spin-gapless semiconductor state for NiCl₃ and *h*-V₂O₃ monolayers [18, 19], topological magnetic-spin textures in Cr₂Ge₂Te₆ [20], spontaneous valley splitting in 2D VAgP₂Se₆ [21], etc. Thus, the rapidly advancing progress in the field of the studies of magnetism in pure 2D materials offers great opportunities for new physical paradigms and next generation information technology [16].

Currently, increased research attention is focused on transition-metal phosphorus trichalcogenides (MPX₃ with M = transition metal and X = S, Se), which crystals can be easily exfoliated into monolayers [22], where a single 2D unit consisting of the transition metal atoms shows honeycomb lattice structure similar to that of graphene (Fig. 1a,b). However, unlike graphene, which has a zero band gap, members of the MPX₃ family demonstrate wide variation of band gaps ranging from 0.5 eV to 3.5 eV [23]. In addition, transition metal compounds have a large spin-orbit coupling and strong electronic correlations compared to the case of graphene.

Overall, due to the diversity of fully or partially occupied *d*-orbitals for the transition metal ions, one may expect a variety of magnetic behavior for MPX₃ monolayers. In this regard, 2D monolayers were studied mostly by theoretical methods, excepting the case of M = Fe for which experimental results are available as well [24]. According to the recent theoretical studies, most of 2D MPX₃ monolayers have antiferromagnetic (AFM) arrangement of magnetic moments of transition metal ions in their ground states [10, 25, 27, 28].

The magnetic phase transition for the MPX₃ materials to the FM state can be realized

(a) CrPSe₃ - top view(b) CrPSe₃ - side view(c) Cr_{1/4}M_{3/4}PSe₃ - top view

● Cr ● M ● P ● Se

FIG. 1: (a,b) Top and side views of the crystal structure of the 2D CrPSe₃ monolayer. (c) Top view of Cr_{1/4}M_{3/4}PSe₃ with the metal ions highlighted. Small shaded rhombus indicates the (1 × 1) unit cell of CrPSe₃. Large dashed rhombus indicates the unit cell of mixed compound, which has a (2 × 2) periodicity with respect to the pristine CrPSe₃. Spheres of different size/color represent ions of different type.

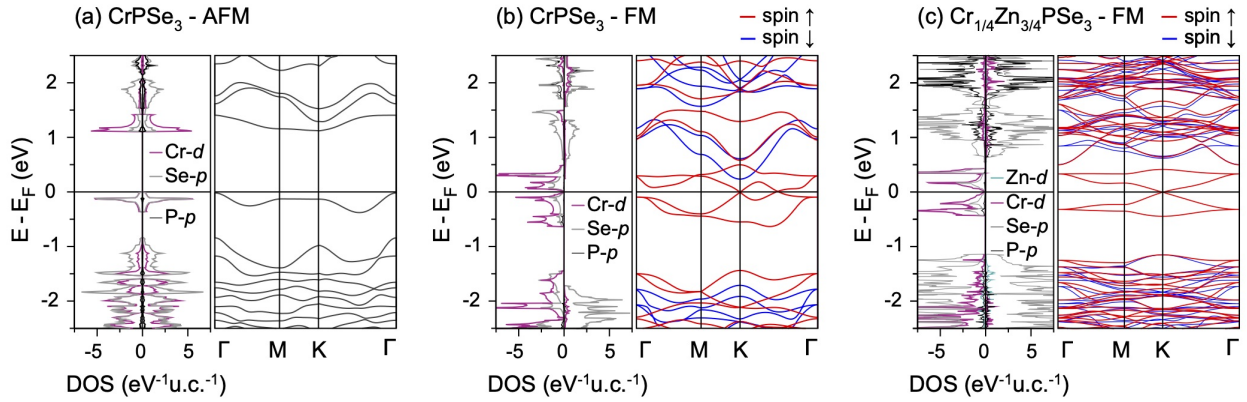


FIG. 2: Band structures and orbital-projected density of states calculated for (a) 2D CrPSe₃ monolayer in the AFM configuration; (b) 2D CrPSe₃ monolayer in the FM configuration; (c) 2D Cr_{1/4}Zn_{3/4}PSe₃ monolayer in the FM configuration.

through applying stress [25] or modulating the carrier concentration [29]. For instance, it was theoretically shown that by means of applying an external voltage gate 2D MnPX_3 ($X = \text{S}, \text{Se}$) can be converted from the AFM semiconducting state into the half-metallic ferromagnetic (HMF) state with $T_C = 206 \text{ K}$ [29]. A further approach to alter the magnetic properties is alloying. Here the properties can be tailored with variation of the concentration of an alloying extent [30, 31].

In this manuscript, the electronic and magnetic properties of 2D CrPSe_3 monolayers are studied using density functional theory including an on-site Coulomb term (DFT+ U) and tight-binding approach (TBA). While CrPSe_3 demonstrates the AFM ground state, its alloying with MPSe_3 ($M = \text{Zn}, \text{Cd}, \text{Hg}$) can be used to stabilize the FM state. $\text{Cr}_{1-x}\text{M}_x\text{PSe}_3$ ($x = 3/4$) is the HMF (Dirac spin-gapless semiconducting) state with near room temperature T_C , obtained in the Monte Carlo simulations. This HMF state emerges Dirac cones in the first 2D Brillouin zone, which originate from the long-range exchange interactions between the d -orbitals of Cr^{2+} ions formed a honeycomb lattice. If spin-orbit coupling (SOC) is taken into account, the $\text{Cr}_{1-x}\text{M}_x\text{PSe}_3$ monolayers become an intrinsic Chern insulators with a large non-trivial band gaps. The high Curie temperature and single-spin Dirac states with high Fermi velocities make 2D $\text{Cr}_{1-x}\text{M}_x\text{PSe}_3$ monolayers very promising materials for low-dimensional spintronics applications.

Our DFT+ U calculations (see Supplemental Material [32] for computational details) show that 2D CrPSe_3 crystal prefers the AFM coupling in its ground state with $T_N = 105 \text{ K}$ (see Tab. S1, Fig. S1, and Fig. S2 in Supplemental Material [32]). The high-spin configuration of Cr^{2+} results in $M_{\text{Cr}} = 3.8 \mu_B$. The calculated electronic band structure indicates that the 2D CrPSe_3 crystal is a semiconductor with an indirect band gap of 1.11 eV (Fig. 2a). Due to the quantum confinement effects this value is slightly larger than the recently published band gap value of a bulk phase (0.70 eV) [33]. The bands in the vicinity of Fermi energy are mostly composed of Cr- d and Se- p orbitals. Hence, the p - d exchange interactions are much weaker than the direct d - d exchange interactions between the NN Cr ions with a bond $d_{\text{Cr-Cr}} = 3.667 \text{ \AA}$, leading to the high negative value of $J_1 = -2.03 \text{ meV}$ (see Supplementary Material [32] for additional theoretical details). For the 2NN and 3NN Cr-ions, the direct d - d interactions decrease significantly with increasing distance between Cr-ions and considerable long-range p - d super-exchange interactions result in positive values of $J_2 = 0.12 \text{ meV}$ and $J_3 = 0.39 \text{ meV}$. Thus, the origin of the AFM ground-state can be attributed to the com-

TABLE I: Results for the 2D CrPSe₃ monolayer and for the 2D Cr_{1/4}M_{3/4}PSe₃ (M = Zn, Cd, Hg) monolayers obtained for the FM state: $\Delta E_{\text{tot}} = E_{\text{FM}} - E_{\text{AFM}}$ (in meV/u.c.) is the energy difference between the FM and AFM states; band gaps, E_g (in meV), are given for the spin-up (\uparrow) and spin-down (\downarrow) channels; J_3 (in meV) is the exchange coupling parameter between two local spins; M_{Cr} (in μ_B) is Cr magnetic moment; T (in K) is a critical temperature; MAE (in meV/u.c.) is magnetic anisotropy energy; v_F (in m/s) is Fermi velocity.

System	ΔE_{tot}	E_g	J_3	M_{Cr}	T	MAE	v_F
CrPSe ₃	285	\uparrow 0/0 ^a (42.8/14.7) ^b ; \downarrow 2079	0.39	3.81	–	650.3	16.11/7.98 ^a $\times 10^5$
Cr _{1/4} Zn _{3/4} PSe ₃	–451	\uparrow 0 (8.6) ^b ; \downarrow 1650	5.03	3.87	264	37.0	3.87 $\times 10^5$
Cr _{1/4} Cd _{3/4} PSe ₃	–416	\uparrow 0 (8.2) ^b ; \downarrow 1660	4.39	3.98	235	119.7	3.98 $\times 10^5$
Cr _{1/4} Hg _{3/4} PSe ₃	–400	\uparrow 0 (6.3) ^b ; \downarrow 970	4.18	3.99	220	87.2	4.03 $\times 10^5$

^aat K and K/2, respectively; ^bfor the data in parenthesis SOC is taken into account

petition between the NN AFM direct Cr–Cr (d – d) exchange interactions and the indirect Cr–Se \cdots Se–Cr (p – d) superexchange interactions.

The FM state of 2D CrPSe₃ is 285 meV higher in energy than the AFM ground-state (Tab. I). Still, it attracts our attention due to its exciting band structure, which demonstrates a half-metallic state with the metallic spin-up channel and insulating spin-down channel (Fig. 2b). For the spin-up electrons, the linear dispersion is observed in the vicinity of the Fermi level and multiple cones appear: one at the K point and an extra one around the midpoint of the $\Gamma - \text{K}$ line named as K/2. The spin-up states near the Fermi level are dominated by Cr- d_{xz} and Cr- d_{yz} orbitals (Fig. 3a), which are hybridized with the p orbitals of Se. The calculations with SOC included lead to the gap opening of 42.8 meV and 14.7 meV for spin-up states at the K and K/2 points, respectively (see Supplemental Material [32] Fig. S3a for the calculated band structures).

In order to better understand the observed phenomena a TBA was applied to the studied system (see Supplementary Material [32] for additional theoretical details). Here the d_{xz} and d_{yz} orbitals can be used as a basis for the honeycomb lattice formed by Cr²⁺ ions and the hopping parameters t_{1j} (NN), t_{2j} (2NN), and t_{3j} (3NN) are marked in Fig. 3e for this

lattice. The modelled band structures are presented in Fig. 3c and they are in reasonable agreement with DFT-calculated band structure (Fig. 3a). Interestingly, the Dirac cones are accurately located at the K point and K/2 midpoint with vertexes just crossed by the Fermi level when considering only the 3NN hopping elements. From a comparison between the two different TBA band structures, the t_{1j} and t_{2j} interactions were found to introduce hole pockets at the K/2 point and electron pockets at the K point, respectively. Since the lattice sites connected by 3NN bonds also form a honeycomb structure with a twice larger lattice constant, the Dirac cones at the K points are folded to the midpoints along the $\Gamma - K$ path. The TBA results confirm that the robust Dirac cones are strongly protected by the lattice symmetry, especially, by the mirror symmetry along the $\Gamma - K$ path. Thus, the origin of the observed Dirac cones can be attributed to the honeycomb lattice structure composed from chromium ions.

In the next step we intend to find a way for stabilisation of the FM state in CrPSe₃. Here we propose to use its alloying with MPSe₃ with M = group-12 metals. The 2D ZnPSe₃, CdPSe₃, and HgPSe₃ are paramagnetic compounds, which correlates with the $d^{10}s^2$ -configuration of Zn, Cd, and Hg. They are semiconductors with the calculated indirect gaps of 1.47 eV, 1.49 eV, 0.83 eV, respectively (see Tab. S2 in Supplemental Material [32]). These DFT+ U values are underestimated with respect to the available experimental data ($E_g^{\text{CdPSe}_3} = 2.29$ eV [34], $E_g^{\text{HgPSe}_3} = 1.95$ eV [35]), but in agreement with the previously published theoretical results [36]. The band edges of these monolayers are composed from Se- p orbitals, whereas the completely filled d -states are strongly localized at around 8 eV below the Fermi level (see Fig. S4 in Supplemental Material [32]).

As shown above, the origin of the AFM ground-state of 2D CrPSe₃ can be attributed to the competition between the NN AFM direct Cr–Cr (d – d) exchange interactions and the indirect Cr–Se \cdots Se–Cr (p – d) superexchange interactions. Consequently, FM may arise when the direct d – d coupling is significantly weakened or even entirely absent. This can be achieved if all nearest-neighbour Cr ions will be substituted by group-12 metal ions, i. e. by means of alloying of CrPSe₃ and MPX₃ with the ratio Cr : M = 1 : 3. The proposed structure for such an alloy is presented in Fig. 1c.

In order to check our idea, we performed the electronic structure calculations for the suggested alloy, i. e. Cr_{1/4}M_{3/4}PSe₃. As expected, all systems under study prefer the FM ground states (Tab. I). In order to further confirm our idea, we carried out similar calcu-

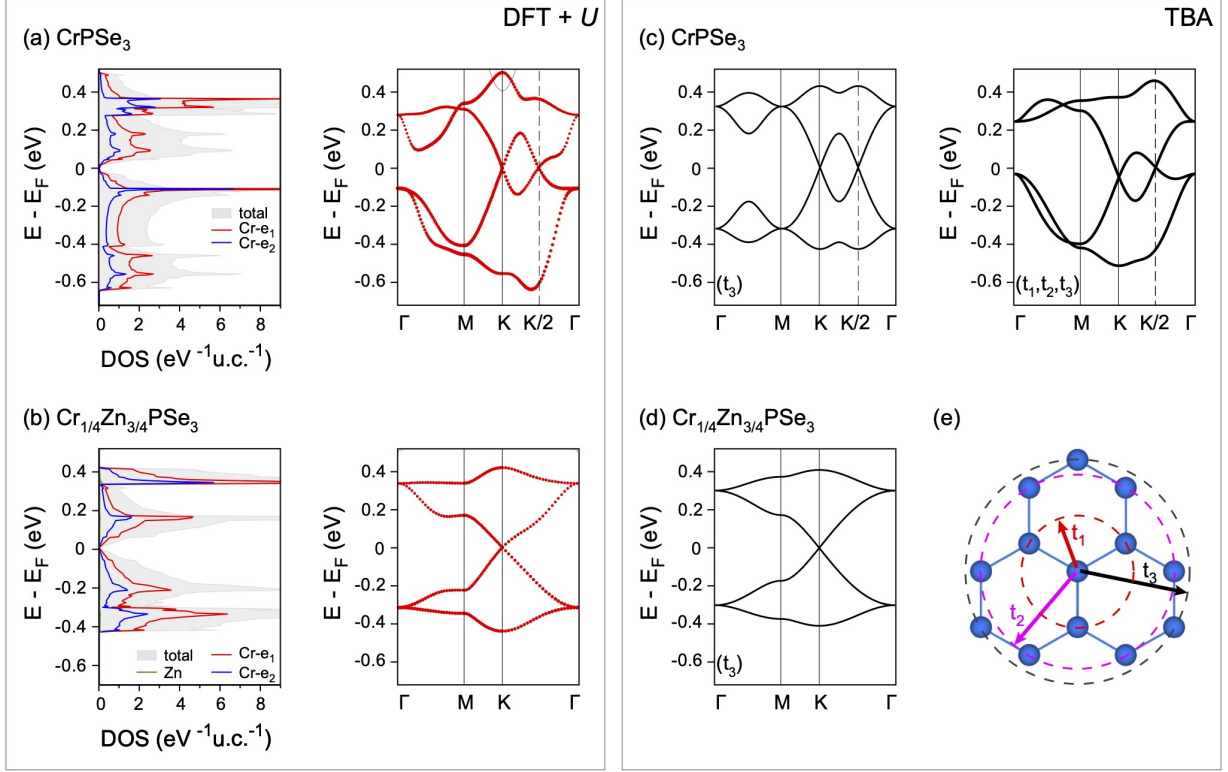


FIG. 3: (a,b) DFT+ U results: (a) Density of states (left) and band structure (right) of the 2D CrPSe₃ monolayer (FM state) in the vicinity of E_F . (b) Density of states (left) and band structure (right) of the 2D Cr_{1/4}Zn_{3/4}PSe₃ monolayer in the vicinity of E_F . Grey shadowed area in DOS shows the total DOS; red and blue lines show the Cr e_1 (d_{xz} , d_{yz}) and Cr e_2 ($d_{x^2-y^2}$, d_{z^2} , d_{xy}) PDOS, respectively; green line corresponds to the Zn d PDOS. In the band structure the weight of the Cr e_1 (d_{xz} , d_{yz}) states is proportional to the width of the colored line. (c-e) TBA results: (c) Bands for 2D CrPSe₃ monolayer when considering either only t_3 hopping elements (left) or t_1 , t_2 , t_3 hopping elements (right). (d) Bands for 2D Cr_{1/4}Zn_{3/4}PSe₃ monolayer. (e) Hopping elements t_1 , t_2 , t_3 .

lations for the opposite case, i.e. Cr_{3/4}M_{1/4}PSe₃, and observed stabilisation of the AFM coupling (see Fig. S5 and Tab. S4 in Supplemental Material [32]). The spin-resolved band structure of Cr_{1/4}Zn_{3/4}PSe₃ in the ground-state configurations is presented in Fig. 2c. The band structures for the cases of M = Cd and Hg show similar behavior and can be seen in Supplemental Material [32] (Fig. S5). All systems under consideration show the HFM behavior with the metallic spin-up channel and insulating spin-down one. The Dirac fermions emerge at the high-symmetry K point in the vicinity of the Fermi level. These Dirac cones

are spin-polarized and resulted from the strong hybridization between Cr-*d* and Se-*p* orbitals. The Cr–Cr interactions are still strong enough in these systems, despite of a long length larger than 7.00 Å for the Cr-honeycomb lattices. Still the FM *p* – *d* superexchange interactions prevail resulting in large J_3 (3NN Cr–Cr pair) values of 5.03 meV, 4.39 meV, and 4.18 meV, obtained for Cr_{1/4}M_{3/4}PSe₃ with M = Zn, Cd, and Hg, respectively (Tab. I). Using the calculated exchange parameters we have employed Monte-Carlo simulations based on the Ising model and estimated Curie temperatures (T_C) (see Supplementary Material [32], Fig. S6). The calculated T_C listed in Tab. I suggest the possibility of using the studied monolayers in near-room temperature spintronics.

The electronic structure of Cr_{1/4}Zn_{3/4}PSe₃ shows rather rare Dirac spin-gapless semiconductor characteristics that are essential for potential high-speed spin filter devices. The calculated Fermi velocities (v_F) in the Γ – K direction for Dirac electrons at the Fermi level are: $3.87 \times 10^5 \text{ m s}^{-1}$, $3.98 \times 10^5 \text{ m s}^{-1}$, and $4.03 \times 10^5 \text{ m s}^{-1}$ for Cr_{1/4}M_{3/4}PSe₃ with M = Zn, Cd, and Hg, respectively. These values for v_F are about a half of the graphene value of $8.2 \times 10^5 \text{ m s}^{-1}$ [37], demonstrating the excellent electronic transport properties of Cr_{1/4}M_{3/4}PSe₃ monolayers. Since the Dirac electrons are derived from the strong *p* – *d* hybridization, the SOC effect was considered to open a band gap. The SOC-induced estimated gaps are 8.6 meV, 8.2 meV and 6.3 meV for Cr_{1/4}M_{3/4}PSe₃ with M = Zn, Cd, and Hg, respectively (see Supplementary Material [32], Fig. S3b-d). These gaps are significantly larger than that of the other Dirac materials, such as graphene [38, 39], which are characterized by Dirac states composed of *p*-orbitals with weak spin-orbital couplings.

As for pristine CrPSe₃, TBA with d_{xz} and d_{yz} orbitals used as a basis for the honeycomb lattice formed by Cr²⁺ ions was applied for the systems under study (see Tab. S3 in Supplementary Material [32]). The band structure obtained for M = Zn is presented in Fig. 3d and it is in a good agreement with DFT-calculated band structure (Fig. 3b). Especially the Dirac cone at the K point as well as the bandwidth calculated with TBA are well reproduced. The hopping parameter t_{11} controls the band width while t_{12} affects the band dispersion, respectively. Some differences between TBA and DFT band structures are caused by the neglecting of the contributions from Se *p* orbitals.

In conclusion, the electronic structure of 2D CrPSe₃ monolayer was explored using first-principles calculations. The calculated band structures obtained on the DFT+*U* level illustrate that the 2D CrPX₃ monolayers adopt the AFM ground state. Simultaneously, its

FM state is half-metallic ferromagnet with multiple spin-polarized Dirac cones. Deep analysis of the observed phenomenon allowed us to find the way to stabilize the FM state by means of alloying of the studied system with MPSe_3 , where M is group-12 metal (Zn, Cd, Hg). Depending on the concentration and location of the alloying extend, it is possible to achieve the HMF Dirac spin-gapless semiconducting state in the FM phase for $\text{Cr}_{1-x}\text{M}_x\text{PSe}_3$ ($x = 3/4$) monolayers. For such cases, the Dirac cone is located at the K point of the Brillouin zone and these fully spin-polarized Dirac cones originate from the long-range exchange interactions between the d -orbitals of Cr^{2+} ions formed a honeycomb lattice. Consequently, SOC opens sizable energy gaps for fully spin-polarized Dirac cones, which are significantly larger compared to the case of Dirac states composed of p -orbitals. The estimated rather high Curie temperatures, large SOC gaps, high Fermi velocities, and single-spin Dirac states for $\text{Cr}_{1-x}\text{M}_x\text{PSe}_3$ ($x = 3/4$) monolayers give rise to great expectations for its potential applications in spintronics.

This work was supported by the National Natural Science Foundation of China (Grant No. 21973059). J.Y. was supported by the Natural Science Foundation of Hubei Province (Grant No. 2018CFB724) and of Education Department (Grant No. D20171803).

-
- [1] K. S. Novoselov, A. K. Geim, S. V. Morozov, D. Jiang, M. I. Katsnelson, I. V. Grigorieva, S. V. Dubonos, and A. A. Firsov, *Nature* **438**, 197 (2005).
 - [2] Y. Zhang, Y.-W. Tan, H. L. Stormer, and P. Kim, *Nature* **438**, 201 (2005).
 - [3] A. K. Geim and K. S. Novoselov, *Nat. Mater.* **6**, 183 (2007).
 - [4] C. Oshima and A. Nagashima, *J. Phys.: Condens. Matter* **9**, 1 (1997).
 - [5] A. A. Tonkikh, E. Voloshina, P. Werner, H. Blumtritt, B. Senkovskiy, G. Güntherodt, S. S. P. Parkin, and Y. S. Dedkov, *Sci. Rep.* **6**, 23547 (2016).
 - [6] K. Zhang, Y. Feng, F. Wang, Z. Yang, and J. Wang, *J. Mater. Chem. C* **5**, 11992 (2017).
 - [7] A. Carvalho, M. Wang, X. Zhu, A. S. Rodin, H. Su, and A. H. Castro Neto, *Nat. Rev. Mater.* **1**, 16061 (2016).
 - [8] M. Houssa, A. Dimoulas, and A. Molle, *J. Phys.: Condens. Matter* **27**, 253002 (2015).
 - [9] A. Molle, C. Grazianetti, L. Tao, D. Taneja, M. H. Alam, and D. Akinwande, *Chem. Soc. Rev.* **47**, 6370 (2018).

- [10] R. Dong and I. Kuljanishvili, J. Vac. Sci. Technol. **35**, 030803 (2017).
- [11] S. Manzeli, D. Ovchinnikov, D. Pasquier, O. V. Yazyev, and A. Kis, Nat. Rev. Mater. **2**, 17033 (2017).
- [12] B. Huang, G. Clark, E. Navarro-Moratalla, D. R. Klein, R. Cheng, K. L. Seyler, D. Zhong, E. Schmidgall, M. A. McGuire, D. H. Cobden, et al., Nature **546**, 270 (2017).
- [13] C. Gong, L. Li, Z. Li, H. Ji, A. Stern, Y. Xia, T. Cao, W. Bao, C. Wang, Y. Wang, et al., Nature **546**, 265 (2017).
- [14] Y. Deng, Y. Yu, Y. Song, J. Zhang, N. Z. Wang, Z. Sun, Y. Yi, Y. Z. Wu, S. Wu, J. Zhu, et al., Nature **563**, 94 (2018).
- [15] D. J. O'Hara, T. Zhu, A. H. Trout, A. S. Ahmed, Y. K. Luo, C. H. Lee, M. R. Brenner, S. Rajan, J. A. Gupta, D. W. McComb, et al., Nano Lett. **18**, 3125 (2018).
- [16] K. S. Burch, D. Mandrus, and J.-G. Park, Nature **563**, 47 (2018).
- [17] M. Gibertini, M. Koperski, A. F. Morpurgo, and K. S. Novoselov, Nature Nanotechnol. **14**, 408 (2019).
- [18] J. He, X. Li, P. Lyu, and P. Nachtigall, Nanoscale **9**, 2246 (2017).
- [19] H. Gog, W.-F. Li, C. Fang, R. S. Koster, M. Dijkstra, and M. Huis, NPJ 2D Mater. Appl. **3**, 18 (2019).
- [20] M.-G. Han, J. A. Garlow, Y. Liu, H. Zhang, J. Li, D. DiMarzio, M. W. Knight, C. Petrovic, D. Jariwala, and Y. Zhu, Nano Lett. **19**, 7859 (2019).
- [21] Z. Song, X. Sun, J. Zheng, F. Pan, Y. Hou, M.-H. Yung, J. Yang, and J. Lu, Nanoscale **10**, 13986 (2018).
- [22] K.-z. Du, X.-z. Wang, Y. Liu, P. Hu, M. I. B. Utama, C. K. Gan, Q. Xiong, and C. Kloc, ACS Nano **10**, 1738 (2016).
- [23] F. Wang, T. A. Shifa, P. Yu, P. He, Y. Liu, F. Wang, Z. Wang, X. Zhan, X. Lou, F. Xia, et al., Adv. Funct. Mater. **28**, 1802151 (2018).
- [24] J. U. Lee, S. Lee, J. H. Ryoo, S. Kang, T. Y. Kim, P. Kim, C.-H. Park, J.-G. Park, and H. Cheong, Nano Lett. **16**, 7433 (2016).
- [25] B. L. Chittari, Y. Park, D. Lee, M. Han, A. H. MacDonald, E. Hwang, and J. Jung, Phys. Rev. B **94**, 184428 (2016).
- [10] N. Sivadas, M. W. Daniels, R. H. Swendsen, S. O. P. R. B, and 2015, Phys. Rev. B **91**, 235425 (2015).

- [27] S. Y. Kim, T. Y. Kim, L. J. Sandilands, S. Sinn, M.-C. Lee, J. Son, S. Lee, K.-Y. Choi, W. Kim, B.-G. Park, et al., *Phys. Rev. Lett.* **120**, 136402 (2018).
- [28] J. Yang, Y. Zhou, Q. Guo, Y. S. Dedkov, and E. Voloshina, *RSC Adv.* **10**, 851 (2020).
- [29] X. Li, X. Wu, and J. Yang, *J. Am. Chem. Soc.* **136**, 11065 (2014).
- [30] T. Masubuchi, H. Hoya, T. Watanabe, Y. Takahashi, S. Ban, N. Ohkubo, K. Takase, and Y. Takano, *J. Alloys Compd.* **460**, 668 (2008).
- [31] D. J. Goossens, S. Brazier-Hollins, D. R. James, W. D. Hutchison, and J. R. Hester, *J. Magn. Magn. Mater.* **334**, 82 (2013).
- [32] See Supplemental Material at <http://XX> for technical details and a complete database of the computational results.
- [33] Y. S. Dedkov, M. Yan, and E. Voloshina, *Chem. Phys. Lett.* **754**, 137627 (2020).
- [34] C. Calareso, V. Grasso, and L. Silipigni, *J. Appl. Phys.* **82**, 6228 (1997).
- [35] C. Calareso, V. Grasso, F. Neri, and L. Silipigni, *J. Phys.: Condens. Matter* **9**, 4791 (1997).
- [36] H. Xiang, B. Xu, Y. Xia, J. Yin, and Z. Liu, *RSC Adv.* **6**, 89901 (2016).
- [37] D. Malko, C. Neiss, F. Viñes, and A. Görling, *Phys. Rev. Lett.* **108**, 086804 (2012).
- [38] M. Gmitra, S. Konschuh, C. Ertler, C. Ambrosch-Draxl, and J. Fabian, *Phys. Rev. B* **80**, 235431 (2009).
- [39] S. Abdelouahed, A. Ernst, J. Henk, I. V. Maznichenko, and U. Starke, *Phys. Rev. B* **82**, 125424 (2010).

Supplementary material for the manuscript: Dirac fermions in half-metallic ferromagnetic mixed $\text{Cr}_{1-x}\text{M}_x\text{PSe}_3$ monolayers

Content:

1. Computational details.
2. Calculation of exchange-coupling parameters: J_1 , J_2 , J_3 .
3. Monte-Carlo simulations.
4. TBA model.
5. Tab. S1: Total energies (E_{tot} , in eV per (2×2) unit cell) as well as total energies relative to that of the lowest-energy magnetic configuration (ΔE , in meV per unit cell) calculated using the PBE+ U ($U = 4$ eV) approximation for the ferromagnetic (FM), Néel antiferromagnetic (AFM), zigzag antiferromagnetic (zAFM), and stripy antiferromagnetic (sAFM) configurations of single-layer CrPSe_3 .
6. Tab. S2: Results for the pristine 2D MPSe_3 monolayers: Ground state magnetic configuration; optimized lattice parameters: in-plane lattice parameter (a), layer thickness (h), M–M and M–Se distances ($d_{\text{M–M}}$ and $d_{\text{M–Se}}$, band gap (E_g).
7. Tab. S3: The hopping parameters, onsite energies and band widths for $\text{Cr}_{1/4}\text{M}_{3/4}\text{PSe}_3$ ($\text{M} = \text{Zn}, \text{Cd}, \text{Hg}$).
8. Tab. S4: Results for the 2D $\text{Cr}_{1-x}\text{M}_x\text{PSe}_3$ ($\text{M} = \text{Zn}, \text{Cd}, \text{Hg}$, $x = 1/4, 3/4$) monolayers obtained for their ground-state states: $\Delta E_{\text{tot}} = E_{\text{FM}} - E_{\text{AFM}}$ (in meV/u.c.) is the energy difference between the FM and AFM states; band gaps, E_g (in eV), are given for the spin-up (\uparrow) and spin-down (\downarrow) channels; $J_{\text{Cr–Cr}}$ (in meV) is the exchange coupling parameter between two local spins; M_{Cr} (in μ_B) is Cr magnetic moment; T (in K) is a critical temperature.
9. Fig. S1: Four different magnetic configurations of 2D CrPSe_3 : (a) ferromagnetic (FM), (b) Néel antiferromagnetic (AFM), (c) zigzag antiferromagnetic (zAFM), and (d) stripy antiferromagnetic (sAFM).
10. Fig. S2: The Monte-Carlo simulated specific heat capacity as a function of temperature for 2D CrPSe_3 .

11. Fig. S3: Comparison of band structures of FM-CrPSe₃ as well as mixed Cr_{1/4}M_{3/4}PSe₃ monolayers in the vicinity of E_F obtained with DFT+ U and with DFT+ U +SOC.
12. Fig. S4: Band structures of 2D MPSe₃ (M = Zn, Cd, Hg).
13. Fig. S5: Band structures and orbital-projected density of states calculated for 2D Cr_{1-x}M_xPSe₃ (M = Zn, Cd, Hg; $x = 1/4, 3/4$) monolayers in their ground-state configurations.
14. Fig. S6: The Monte-Carlo simulated specific heat capacity as a function of temperature for 2D Cr_{1/4}M_{3/4}PSe₃ (M = Zn, Cd, Hg).

1. Computational details

Spin-polarised DFT calculations based on plane-wave basis sets of 500 eV cutoff energy were performed with the Vienna *ab initio* simulation package (VASP) [1–3]. The Perdew-Burke-Ernzerhof (PBE) exchange-correlation functional [4] was employed. The electron-ion interaction was described within the projector augmented wave (PAW) method [5] with Cr ($3p, 3d, 4s$), P ($3s, 3p$), and Se ($4s, 4p$) states treated as valence states. The Brillouin-zone integration was performed on Γ -centred symmetry reduced Monkhorst-Pack meshes using a Gaussian smearing with $\sigma = 0.05$ eV, except for the calculation of total energies. For these calculations, the tetrahedron method with Blöchl corrections [6] was employed. A $12 \times 12 \times 1$ k -mesh was used in the case of ionic relaxations and $24 \times 24 \times 1$ for single point calculations, respectively. The DFT+ U scheme [7, 8] was adopted for the treatment of Cr $3d$ orbitals, with the parameter $U_{\text{eff}} = U - J$ equal to 4 eV. Dispersion interactions were considered adding a $1/r^6$ atom-atom term as parameterised by Grimme (“D2” parameterisation) [9]. To ensure decoupling between periodically repeated layers, a vacuum space of 20 Å was used. During structure optimisation, the convergence criteria for energy and force were set equal to 10^{-6} eV and 1×10^{-2} eV/Å, respectively.

2. Calculation of exchange-coupling parameters: J_1 , J_2 , J_3

The magnetic coupling parameter J can be extracted by mapping the total energies of four spin orders (Fig.) to the Ising model with a Hamiltonian

$$H = \sum_{\langle i,j \rangle} J_1 \vec{S}_i \cdot \vec{S}_j + \sum_{\langle\langle i,j \rangle\rangle} J_2 \vec{S}_i \cdot \vec{S}_j + \sum_{\langle\langle\langle i,j \rangle\rangle\rangle} J_3 \vec{S}_i \cdot \vec{S}_j,$$

where \vec{S}_i is the net spin magnetic moment of the Cr ions at site i , three different distance magnetic coupling parameters were estimated, considering one central Cr ions interacted with three nearest neighbouring (NN, J_1), six next-nearest neighbouring (2NN, J_2), and three third-nearest neighbouring (3NN, J_3) Cr ions, respectively.

The long-range magnetic exchange parameters (J) can be obtained as [10]

$$\begin{aligned} J_1 &= \frac{E_{\text{FM}} - E_{\text{AFM}} + E_{\text{zAFM}} - E_{\text{sAFM}}}{8S^2}, \\ J_2 &= \frac{E_{\text{FM}} + E_{\text{AFM}} - (E_{\text{zAFM}} + E_{\text{sAFM}})}{16S^2}, \\ J_3 &= \frac{E_{\text{FM}} - E_{\text{AFM}} - 3(E_{\text{zAFM}} - E_{\text{sAFM}})}{24S^2}. \end{aligned}$$

For the mixed compound, considering only one possible magnetic interaction, the exchange parameters are calculated as $J = \Delta E / 6S^2$, where ΔE is the energy difference between the FM and AFM orders: $\Delta E = E_{\text{FM}} - E_{\text{AFM}}$.

3. Monte-Carlo simulations

To estimate T_N and T_C temperatures, Monte-Carlo (MC) simulations were performed within the Metropolis algorithm with periodic boundary conditions [11].

Using the exchange parameters, MC simulations based on the Ising model were then carried out to evaluate the Néel temperatures in a 32×32 2D superlattice using at least 10^9 steps. In each step, the spins on all the sites in the superlattice flip randomly according to the spin states. The specific heat capacity $C_v(T) = (\langle E^2 \rangle - \langle E \rangle^2)/k_B T^2$ as a function of temperature were calculated. The critical temperatures were extracted from the peak position of the specific heat capacity $C_v(T)$.

4. TBA model

The effective Hamiltonian can be denoted as [12]

$$H_0 = \sum_k \psi_k^\dagger h_k \psi_k = \sum_{\kappa\alpha\beta} \sum_{\mu\nu} h_{\mu\nu}^{\alpha\beta}(\kappa) c_{\alpha\mu}^\dagger c_{\beta\nu}.$$

Here μ, ν indicate the orbitals (d_{xy}, d_{yz}), and α, β indicate two sublattices with different orientations (A, B). The basis $\psi_k = (c_{\kappa,A,xz}^\dagger, c_{\kappa,A,yz}^\dagger, c_{\kappa,B,xz}^\dagger, c_{\kappa,B,yz}^\dagger)$ with the electron creation operator $c_{\alpha\mu}^\dagger$ means creating an electron for μ orbital with momentum \mathbf{k} in α sublattice. The 4×4 basis $h(\kappa)$ is described as

$$h(k) = \begin{pmatrix} \omega - \epsilon & \gamma \\ \gamma^\dagger & \omega^T - \epsilon \end{pmatrix}$$

where ϵ is onsite energy, $T = C_j T^i C_j^{-1}$ is a 2×2 matrix of the hopping parameter t_{ij} with a three-fold rotation operation C_j to the ij hopping direction between the manifold of d orbitals. The element $\omega_k = \sum_{\langle\langle i,j \rangle\rangle} e^{-i\mathbf{k} \cdot \mathbf{a}_{2j}} T_j^{2NN}$ is the summation of Fourier transform of t_{2j} hopping matrix with 2NN neighboring vector \mathbf{a}_2 , similarly γ refers to the summations of t_{1j} and 3NN t_{3j} hopping matrices Fourier transformation.

The matrix elements of the 4×4 Hamiltonian are

$$h_{11} = 2t_{21} \cos^2 \frac{k_x}{2} + (t_{21} + 3t_{23}) \cos \frac{k_x}{2} \cos \frac{\sqrt{3}k_y}{2} - 2t_{21} \sin^2 \frac{k_x}{2},$$

$$h_{12} = \sin \frac{k_x}{2} [4it_{22} \cos \frac{k_x}{2} - 4it_{22} \cos \frac{\sqrt{3}k_y}{2} + \sqrt{3}(-t_{21} + t_{23}) \sin \frac{\sqrt{3}k_y}{2}],$$

$$\begin{aligned} h_{13} = & \frac{1}{2} (\cos \frac{k_y}{2\sqrt{3}} - i \sin \frac{k_y}{2\sqrt{3}}) (t_{11} + 3t_{12}) \cos \frac{k_x}{2} \\ & + \frac{1}{2} (\cos \frac{k_y}{2\sqrt{3}} - i \sin \frac{k_y}{2\sqrt{3}}) [i(2(t_{11} - t_{31}) + (t_{31} + 3t_{32}) \cos k_x) \sin \frac{\sqrt{3}k_y}{2} \\ & + \frac{1}{2} (\cos \frac{k_y}{2\sqrt{3}} - i \sin \frac{k_y}{2\sqrt{3}}) [2(t_{11} + t_{31}) + (t_{31} + 3t_{32}) \cos k_x] \cos \frac{\sqrt{3}k_y}{2}, \end{aligned}$$

$$\begin{aligned} h_{14} = & \frac{\sqrt{3}}{2} [i(t_{11} - t_{12}) \cos \frac{k_y}{2\sqrt{3}} \sin \frac{k_x}{2} - i(t_{31} - t_{32}) \cos^2 \frac{k_y}{2\sqrt{3}} \sin k_x \\ & + (t_{11} - t_{12}) \sin \frac{k_x}{2} \sin \frac{k_y}{2\sqrt{3}} - \frac{1}{2} i(t_{31} - t_{32}) (\cos \frac{k_y}{\sqrt{3}} \sin k_x + 2i \sin \frac{k_y}{\sqrt{3}} \sin k_x - \sin k_x)], \end{aligned}$$

$$h_{22} = 2t_{23} \cos^2 \frac{k_x}{2} + (t_{23} + 3t_{21}) \cos \frac{k_x}{2} \cos \frac{\sqrt{3}k_y}{2} - 2t_{23} \sin^2 \frac{k_x}{2},$$

$$h_{24} = \frac{1}{2} \left(\cos \frac{k_y}{2\sqrt{3}} - i \sin \frac{k_y}{2\sqrt{3}} \right) \left[(3t_{11} + t_{12}) \cos \frac{k_x}{2} + (2(t_{12} + t_{32}) + (3t_{31} + t_{32}) \cos k_x) \cos \frac{\sqrt{3}k_y}{2} \right] \\ + \frac{1}{2} \left(\cos \frac{k_y}{2\sqrt{3}} - i \sin \frac{k_y}{2\sqrt{3}} \right) \left[2i(t_{12} - t_{32}) + i(3t_{31} + t_{32}) \cos k_x \sin \frac{\sqrt{3}k_y}{2} \right]$$

Here, $h_{33} = h_{11}$, $h_{44} = h_{22}$, $h_{23} = h_{14}$ and $h_{34} = h_{12}^*$.

The hopping parameters for TBA were evaluated by Wannier90 program [13].

The three-different distance hopping parameters of 2D CrPSe₃ are $t_{11} = -0.066969$, $t_{12} = -0.048230$, $t_{21} = 0.016447$, $t_{22} = -0.002230$, $t_{23} = 0.0020415$, $t_{31} = -0.034616$, and $t_{32} = 0.241613$, respectively, and the onsite energies are $\epsilon_{xxzz} = -2.275418$ eV and $\epsilon_{yzyz} = -2.274829$ eV. Considering only the NN interactions ($t_{2j} = t_{3j} = 0$), the hopping parameters and chemical potentials of M_{1/4}Zn_{3/4}PSe₃ are listed in Tab. S3, respectively.

TABLE II: Total energies (E_{tot} in eV per (2×2) unit cell) as well as total energies relative to that of the lowest-energy magnetic configuration (ΔE , in meV per unit cell) calculated using the DFT+ U ($U = 4$ eV) approximation for the ferromagnetic (FM), Néel antiferromagnetic (AFM), zigzag antiferromagnetic (zAFM), and stripy antiferromagnetic (sAFM) configurations of single-layer CrPSe₃.

Energy	FM	AFM	zAFM	sAFM
E_{tot}	-204.016	-204.301	-204.040	-204.224
ΔE	285	0	261	77

TABLE III: Results for the pristine 2D MPSe₃ monolayers: Ground state magnetic configuration; optimized lattice parameters: in-plane lattice parameter (a), layer thickness (h), M–M and M–Se distances ($d_{\text{M–M}}$ and $d_{\text{M–Se}}$), band gap (E_g).

System	State	a (Å)	h (Å)	$d_{\text{M–M}}$ (Å)	$d_{\text{M–Se}}$ (Å)	E_g (eV)
CrPSe ₃	AFM	6.352	3.534	3.667	2.727	1.11
ZnPSe ₃	NM	6.291 (6.290 [14])	3.374	3.662	2.839	1.47
CdPSe ₃	NM	6.515	3.580	3.761	2.839	1.49
HgPSe ₃	NM	6.550 (6.545 [15])	3.633	3.782	2.873	0.83

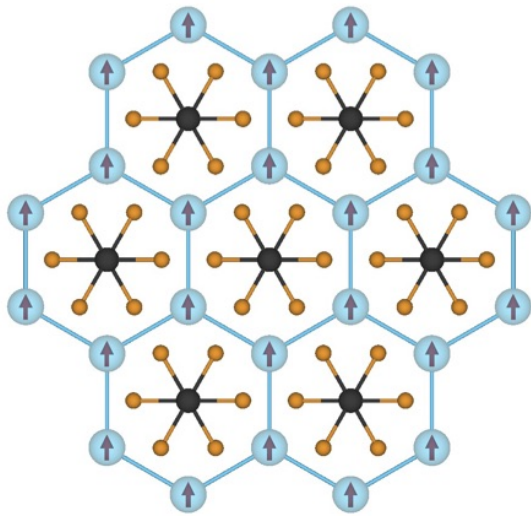
TABLE IV: The hopping parameters, onsite energies and band widths for $\text{Cr}_{1/4}\text{M}_{3/4}\text{PSe}_3$ (M = Zn, Cd, Hg).

System	Hopping parameter (eV)		ϵ (eV)		Band width (eV)	
	t_{11}	t_{22}	h_{xxxz}	h_{yyyz}	TBA	DFT
$\text{Cr}_{1/4}\text{Zn}_{3/4}\text{PSe}_3$	0.236657	-0.036112	-2.299083	-2.298403	0.82	0.87
$\text{Cr}_{1/4}\text{Cd}_{3/4}\text{PSe}_3$	0.213962	-0.033283	-2.757786	-2.757788	0.74	0.77
$\text{Cr}_{1/4}\text{Hg}_{3/4}\text{PSe}_3$	0.209113	-0.028072	-2.815065	-2.814500	0.71	0.73

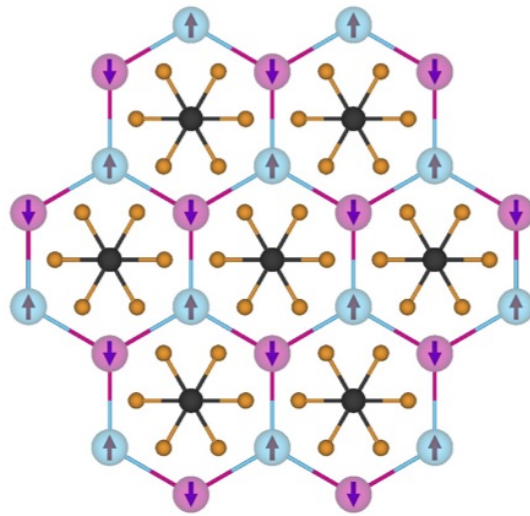
TABLE V: Results for the 2D $\text{Cr}_{1-x}\text{M}_x\text{PSe}_3$ ($\text{M} = \text{Zn}, \text{Cd}, \text{Hg}$, $x = 1/4, 3/4$) monolayers obtained for their ground-state states: $\Delta E_{\text{tot}} = E_{\text{FM}} - E_{\text{AFM}}$ (in meV/u.c.) is the energy difference between the FM and AFM states; band gaps, E_g (in eV), are given for the spin-up (\uparrow) and spin-down (\downarrow) channels; $J_{\text{Cr-Cr}}$ (in meV) is the exchange coupling parameter between two local spins; M_{Cr} (in μ_B) is Cr magnetic moment; T (in K) is a critical temperature.

M	x	ΔE_{tot}	E_g	$J_{\text{Cr-Cr}}$	M_{Cr}	T
Zn	3/4	-451	\uparrow 0 \downarrow 1.65	5.03	3.87	264
	1/4	346	0.78	-4.22		
Cd	3/4	-416	\uparrow 0, \downarrow 1.66	4.39	3.98	235
	1/4	578	0.90	-6.57		
Hg	3/4	-400	\uparrow 0, \downarrow 0.97	4.18	3.99	220
	1/4	592	0.87	-7.21		

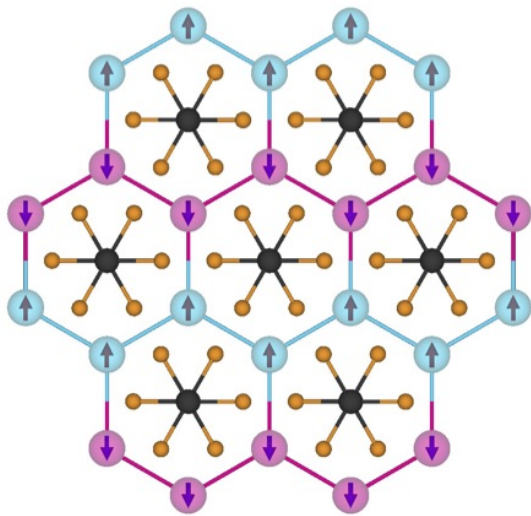
(a) FM



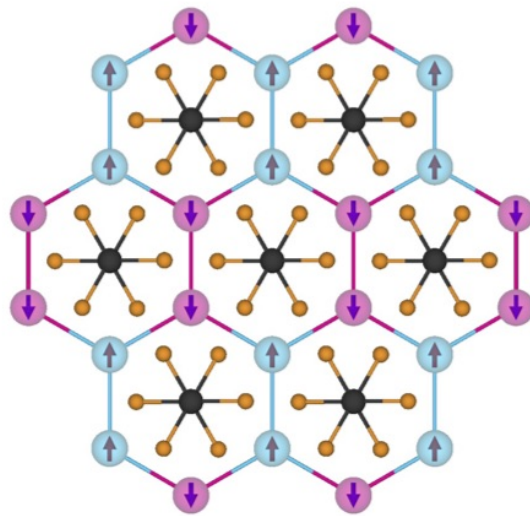
(b) AFM



(c) zAFM



(d) sAFM



↑ spin-up

↓ spin-down

Fig. S1. Four different magnetic configurations of 2D CrPSe₃: (a) ferromagnetic (FM), (b) Néel antiferromagnetic (AFM), (c) zigzag antiferromagnetic (zAFM), and (d) stripy antiferromagnetic (sAFM).

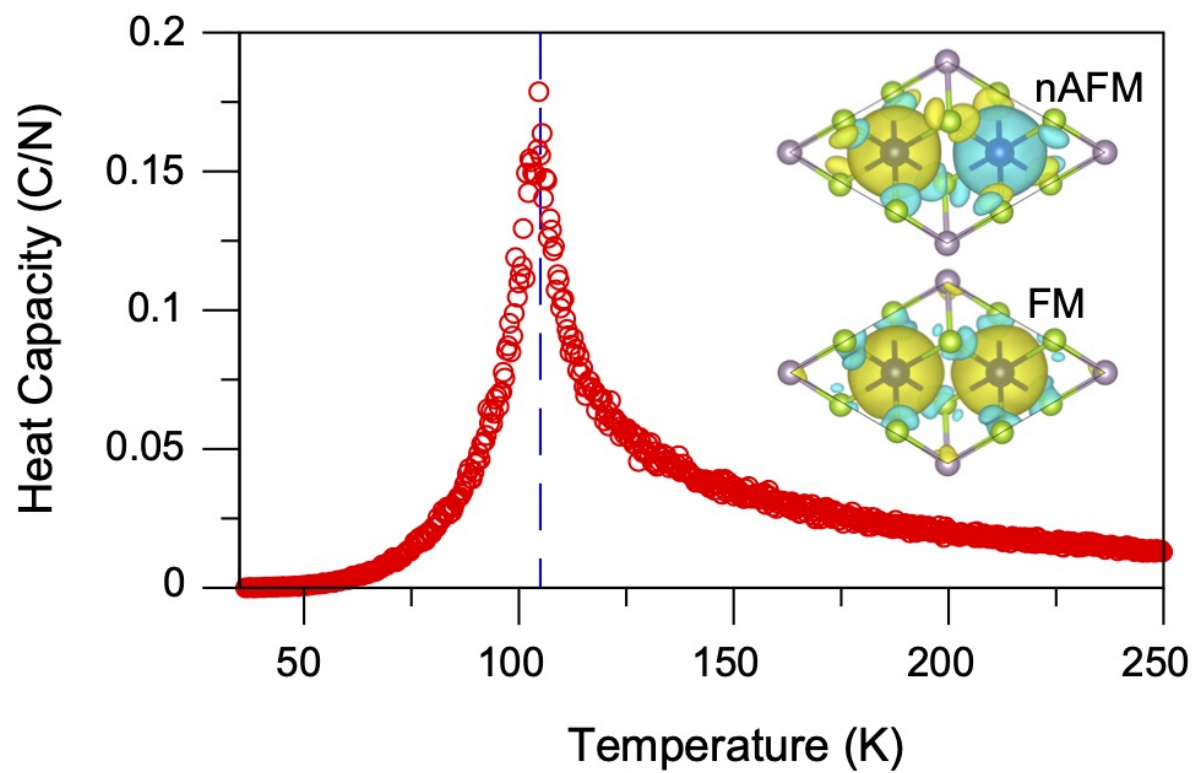


Fig. S2. The Monte-Carlo simulated specific heat capacity as a function of temperature for 2D CrPSe₃.

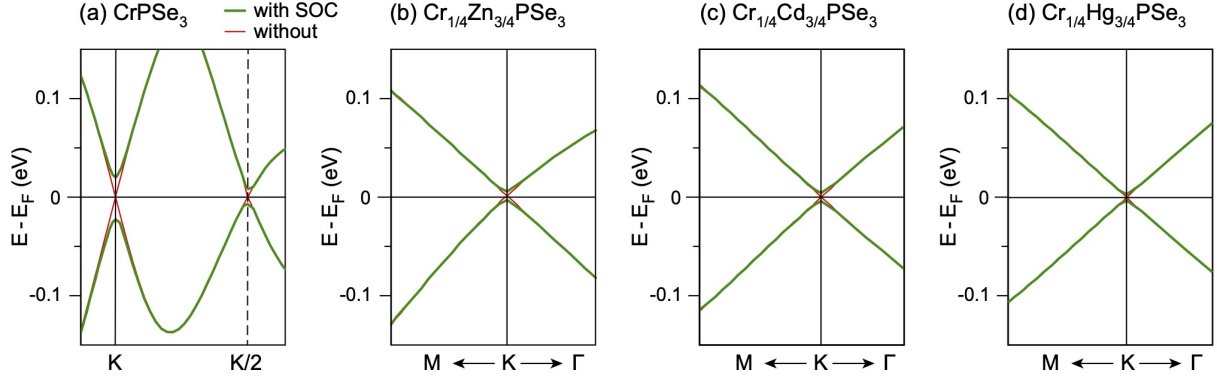


Fig. S3. Comparison of band structures of FM- CrPSe_3 as well as mixed $\text{Cr}_{1/4}\text{M}_{3/4}\text{PSe}_3$ monolayers in the vicinity of E_F obtained with DFT+ U and with DFT+ U +SOC.

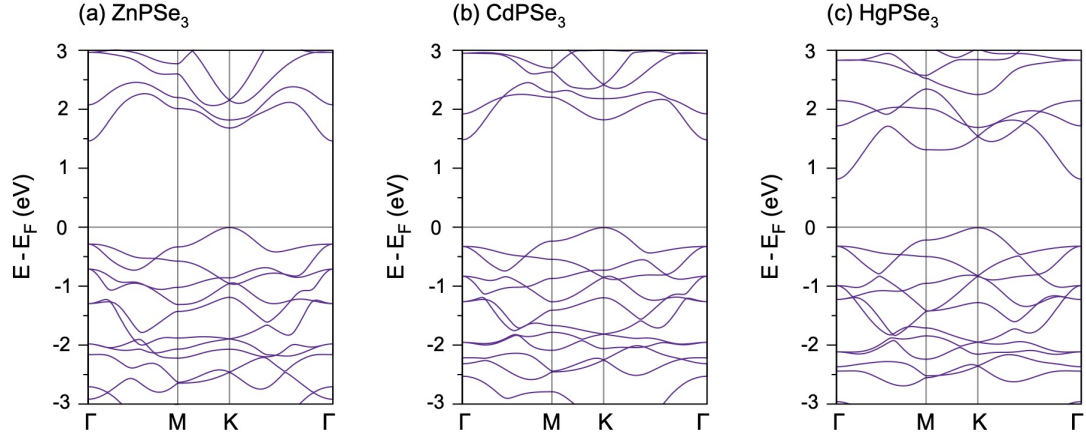


Fig. S4. Band structures of 2D MPSe_3 ($M = \text{Zn, Cd, Hg}$).

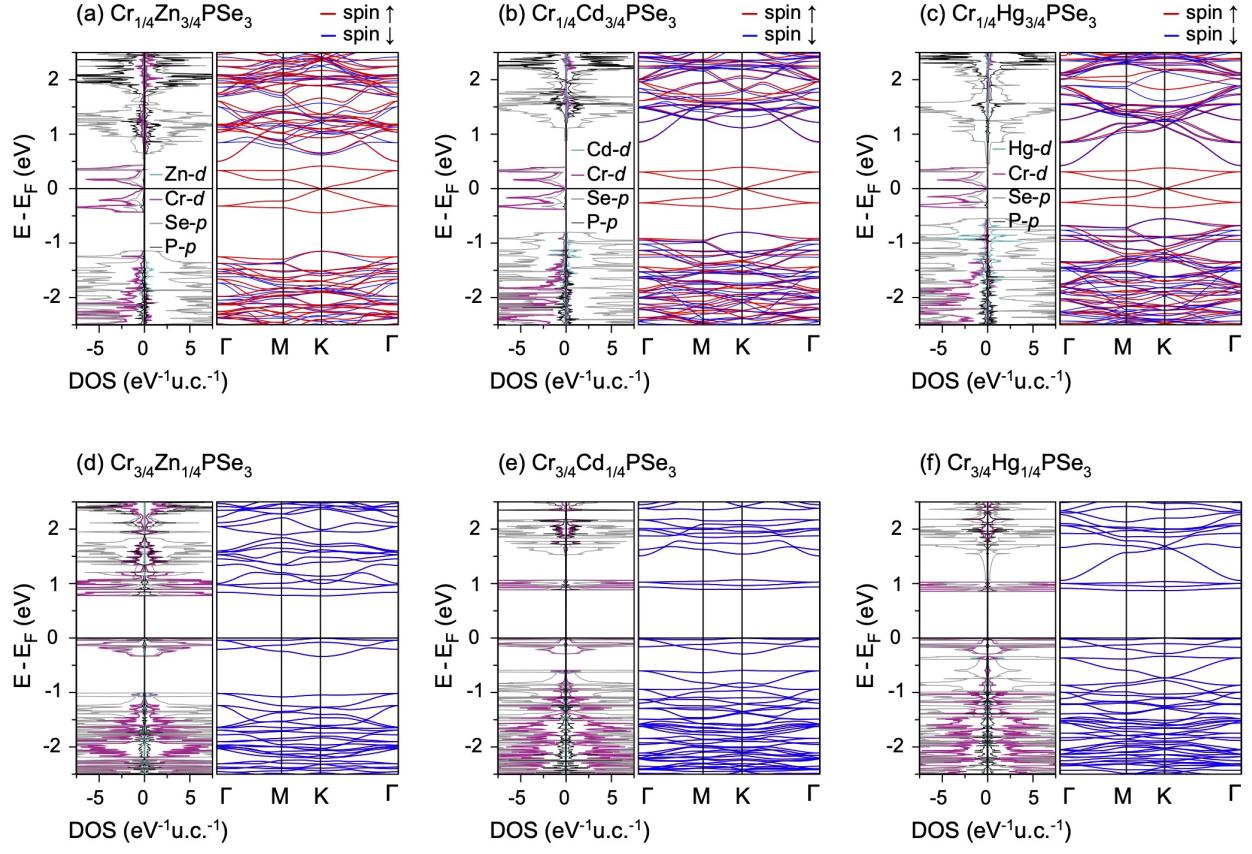


Fig. S5. Band structures and orbital-projected density of states calculated for 2D $\text{Cr}_{1-x}\text{M}_x\text{PSe}_3$ ($\text{M} = \text{Zn}, \text{Cd}, \text{Hg}; x = 1/4, 3/4$) monolayers in their ground-state configurations.

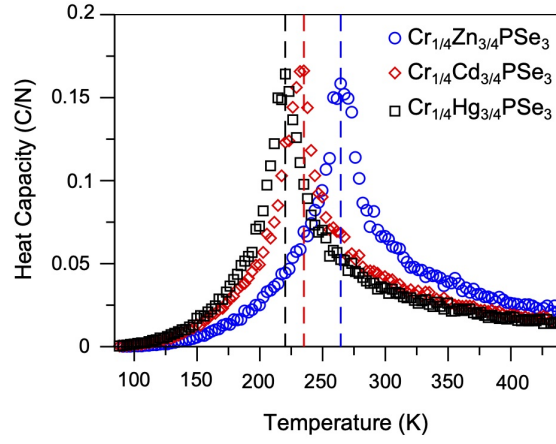


Fig.S6. The Monte-Carlo simulated specific heat capacity as a function of temperature for 2D $\text{Cr}_{1/4}\text{M}_{3/4}\text{PSe}_3$ ($\text{M} = \text{Zn}, \text{Cd}, \text{Hg}$).

-
- [1] G. Kresse and J. Furthmüller, *Comp. Mater. Sci.* **6**, 15 (1996).
 - [2] G. Kresse and J. Hafner, *J. Phys.: Condens. Matter* **6**, 8245 (1994).
 - [3] G. Kresse and J. Hafner, *Phys. Rev. B* **47**, 558 (1993).
 - [4] J. P. Perdew, K. Burke, and M. Ernzerhof, *Phys. Rev. Lett.* **78**, 1396 (1997).
 - [5] P. E. Blöchl, *Phys. Rev. B* **50**, 17953 (1994).
 - [6] P. E. Blöchl, O. Jepsen, and O. K. Andersen, *Phys. Rev. B* **49**, 16223 (1994).
 - [7] V. I. Anisimov, F. Aryasetiawan, and A. I. Lichtenstein, *J. Phys.: Condens. Matter* **9**, 767 (1997).
 - [8] S. L. Dudarev, G. A. Botton, S. Y. Savrasov, C. J. Humphreys, and A. P. Sutton, *Phys. Rev. B* **57**, 1505 (1998).
 - [9] S. Grimme, *J. Comput. Chem.* **27**, 1787 (2006).
 - [10] N. Sivadas, M. W. Daniels, R. H. Swendsen, S. O. P. R. B, and 2015, *Phys. Rev. B* **91**, 235425 (2015).
 - [11] N. Metropolis, A. W. Rosenbluth, M. N. Rosenbluth, A. H. Teller, and E. Teller, *J. Chem. Phys.* **21**, 1087 (1953).
 - [12] Y. Gu, Q. Zhang, C. Le, Y. Li, T. Xiang, and J. Hu, *Phys. Rev. B* **100**, 165405 (2019).
 - [13] G. Pizzi, V. Vitale, R. Arita, S. Bluegel, F. Freimuth, G. Géranton, M. Gibertini, D. Gresch, C. Johnson, T. Koretsune, et al., *J. Phys.: Condens. Matter* pp. 1–62 (2019).
 - [14] S. Jörgens and A. Mewis, *Z. Anorg. Allg. Chem.* **630**, 51 (2004).
 - [15] M. Z. Jandali, G. Eulenberger, and H. Hahn, *Z. Anorg. Allg. Chem.* **447**, 105 (1978).